Earth and Planetary Science Letters 442 (2016) 1–12

Contents lists available at ScienceDirect

Earth and Planetary Science Letters

www.elsevier.com/locate/epsl

Permeability control on transient slip weakening during gypsum dehydration: Implications for earthquakes in subduction zones

Henri Leclère *, Daniel Faulkner, John Wheeler, Elisabetta Mariani

Department of Earth and Ocean Sciences, University of Liverpool, 4 Brownlow Street, Liverpool, L69 3GP, UK

ARTICLE INFO

Article history:
Received 9 October 2015
Received in revised form 20 January 2016
Accepted 5 February 2016
Available online xxxx
Editor: J. Brodholt

Keywords:
gypsum dehydration
Riedel shear
permeability
slip weakening
pore-fluid pressure

ABSTRACT

A conflict has emerged from recent laboratory experiments regarding the question of whether or not dehydration reactions can promote unstable slip in subduction zones leading to earthquakes. Although reactions produce mechanical weakening due to pore-fluid pressure increase, this weakening has been associated with both stable and unstable slip. Here, new results monitoring strength, permeability, pore-fluid pressure, reaction progress and microstructural evolution during dehydration reactions are presented to identify the conditions necessary for mechanical instability. Triaxial experiments are conducted using gypsum and a direct shear sample assembly with constant normal stress that allows the measurement of permeability during sliding. Tests are conducted with temperature ramp from 70 to 150 °C and with different effective confining pressures (50, 100 and 150 MPa) and velocities (0.1 and 0.4 $\mu m\,s^{-1}$). Results show that gypsum dehydration to bassanite induces transient stable-slip weakening that is controlled by pore-fluid pressure and permeability evolution. At the onset of dehydration, the low permeability promoted by pore compaction induces pore-fluid pressure build-up and stable slip weakening. The increase of bassanite content during the reaction shows clear evidence of dehydration related with the development of R_1 Riedel shears and P foliation planes where bassanite is preferentially localized along these structures. The continued production of bassanite, which is stronger than gypsum, provides a supporting framework for newly formed pores, thus resulting in permeability increase, pore-fluid pressure drop and fault strength increase. After dehydration reaction, deformation is characterized by unstable slip on the fully dehydrated reaction product, controlled by the transition from velocity-strengthening to velocity-weakening behaviour of bassanite at temperature above ~140 °C and the localization of deformation along narrow Y-shear planes. This study highlights the generic conditions required to trigger instabilities during dehydration reactions. It shows that pore-fluid pressure build-up during dehydration reactions associated with the localization of a velocity-weakening reacting or dehydrated phase along shear planes is necessary for earthquake triggering.

1. Introduction

The understanding of fault mechanics is of first order importance to unravel earthquake triggering. Among the parameters promoting fault reactivation and earthquake triggering, the influence of pore-fluid pressure and friction on stability of fault zones has been a focus of recent work based on geological, geophysical and experimental analyses. Many authors have dealt with mechanisms promoting fault reactivation such as the reduction of friction coefficient due to mineralogical and/or microstructural transformations (Collettini et al., 2009) or the increase of pore-fluid pressure in fault zones by fault compaction or devolatilization (Sleep and Blanpied, 1992; Ko et al., 1997; Wong et al., 1997; Leclère et al., 2015). Dehydration reactions combine these two mechanisms due to mineral phase changes and free-water release during reaction. The interest in how mechanical behaviour is affected by dehydration reactions is fuelled by the desire to understand and explain the strong correlation between the location of dehydration reactions along subduction zones and intermediate depth earthquakes (50 to 200 km) (Peacock, 2001; Hacker et al., 2003; Nakajima et al., 2009; Abers et al., 2013). However, key questions still remain, such as recent work that has highlighted a conflict surrounding whether or not dehydration reactions can promote instability in subduction zones where dehydration occurs (Proctor and Hirth, 2015).

Many studies conducted in the laboratory have focused on the modifications of hydro-mechanical properties during dehydration reactions. The concept of dehydration embrittlement was intro-

* Corresponding author. Tel.: +44 (0)151 794 5149.
E-mail address: henri.leclere@liverpool.ac.uk (H. Leclère).

http://dx.doi.org/10.1016/j.epsl.2016.02.015

duced by Raleigh and Paterson (1965) and was proposed as a mechanism to explain the triggering of earthquakes during dehydration reactions in subduction zones. A key issue is that, at the very high pressures in the intermediate depth range (50–200 km), pressure-sensitive brittle behaviour would be inhibited and brittle instability would be suppressed (Hilairet et al., 2007). Dehydration embrittlement can circumvent this problem by the build up of pore-fluid pressure during the release of free-water, reducing the effective stress and allowing brittle behaviour to occur (Raleigh and Paterson, 1965; Dobson et al., 2002; Jung et al., 2004). However, recent laboratory dehydration experiments have led to conflicting views on whether the brittle behaviour promoted by dehydration embrittlement can result in earthquake triggering. These studies can be broadly divided in two categories: (1) studies documenting brittle instability and stick–slip events during dehydration reactions (Shimamoto, 1986; Milsch and Scholz, 2005; Takahashi et al., 2011; Okazaki and Katayama, 2015) and (2) studies documenting stable slip during dehydration reactions (Chernak and Hirth, 2011; Proctor and Hirth, 2015).

Dehydration embrittlement has been observed from thin sections or recorded using acoustic emissions sensors during experiments (Raleigh and Paterson, 1965; Dobson et al., 2002; Jung et al., 2004; Burlini et al., 2009; Brantut et al., 2012). Dramatic stick–slip events have been also recorded during dehydration reactions using a saw cut geometry with serpentine and gypsum leading to the conclusion that dehydration reactions can trigger earthquakes (Shimamoto, 1986; Milsch and Scholz, 2005; Takahashi et al., 2011; Okazaki and Katayama, 2015). Takahashi et al. (2011) explained stick–slip events recorded during their triaxial experiments at constant pore pressure ($PP = 30$ MPa) and confining pressure ($PC = 100$ MPa) by the preferential localization of dehydrated products (*i.e.* olivine) along frictional shear planes. Conversely, Chernak and Hirth (2011) and Proctor and Hirth (2015), using a Griggs type-apparatus, recorded stable sliding during serpentine dehydration associated with distributed semi-brittle deformation at antigorite dehydration conditions. From the studies above it is clear that the understanding of strain localization during metamorphism and the conditions leading to unstable frictional sliding along localized zones is of primary importance (Proctor and Hirth, 2015).

This study is focused on the links between dehydration reactions, slip weakening and localization of deformation, as well as the question of slip instability, using gypsum as an analogue for dehydrating systems. A direct shear sample assembly allowing constant normal stress and control of the pore-fluid pressure is used during the experiments. This study goes beyond the work conducted by Proctor and Hirth (2015) who showed that slip weakening during serpentine dehydration is qualitatively controlled by how well drained the sample is. In the experiments presented here, the evolution of pore-fluid pressure and permeability, in addition to the shear stress, were measured continuously throughout the experiment until dehydration reaction reached completion. Our study shows that slip weakening is transient and is controlled by permeability and pore-fluid pressure evolution during dehydration reactions. Transient slip weakening is characterized by stable slip weakening followed by fault strength recovery and unstable, stick–slip behaviour on fully dehydrated material. Microstructural analyses conducted on deformed samples show clear evidence of dehydration reactions related to the development of R_1 Riedel shears and P foliation planes. A conceptual model is then proposed to explain transient slip weakening during gypsum dehydration incorporating the key role played by permeability. This model provides a framework to define the conditions required to trigger unstable events during dehydration reactions.

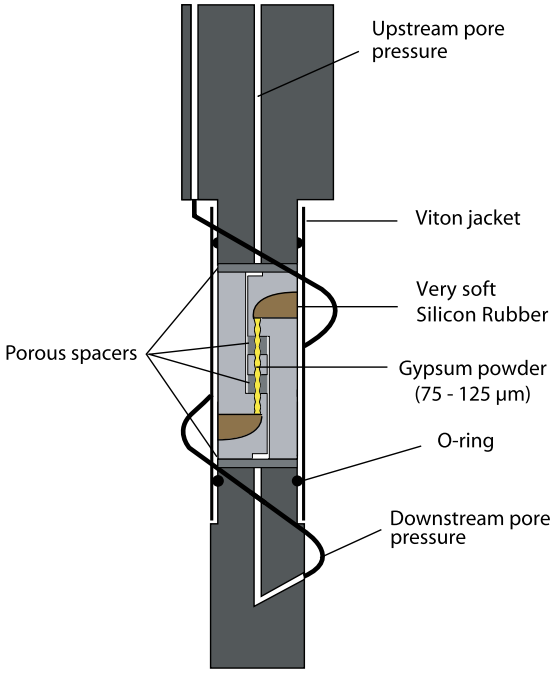

Fig. 1. Schematic diagram of the direct shear sample assembly used in this study.

2. Starting material and experimental setup

2.1. Experimental procedure

Volterra gypsum powder with a grain size ranging from 75 to 125 μm was sheared within a conventional triaxial apparatus using a direct shear sample assembly similar to that used by Verberne et al. (2013) (Fig. 1). Experiments were conducted at one of two controlled slip velocities of 0.1 or 0.4 $\mu m\,s^{-1}$ corresponding respectively to a strain rate of $0.3 \times 10^{-5}\ s^{-1}$ and $1.3 \times 10^{-5}\ s^{-1}$, and with a constant temperature ramp of respectively 0.125 and 0.5 $^{\circ}C\,min^{-1}$ between 70 and 150 °C. The ratio between strain rate and heating rate was kept constant in all experiments and is comparable to those observed in subduction zones (Chernak and Hirth, 2011). Temperature ramps were applied after 1 mm of displacement after the yield point was reached. During the first millimetre of displacement, temperature is kept constant at 70 °C, below the start of dehydration, and the velocity is kept at 0.4 $\mu m\,s^{-1}$ before applying the temperature ramp and changing velocity for experiments conducted at 0.1 $\mu m\,s^{-1}$. The influence of slip velocity (V) and effective confining pressure (PC_{eff}) are analysed for 6 experiments by modifying PC_{eff} (50, 100 and 150 MPa) and V (0.1 and 0.4 $\mu m\,s^{-1}$) (see Table 1). Then, another 4 experiments with conditions equivalent to those of DS20 were run, but halted at different displacements so that microstructural evolution could be determined. Experiments were conducted under semi-undrained conditions where the pore-fluid pressure is only controlled on one side of the sample with a mean pore pressure of 2 MPa. The other side of the shearing layer is connected to a fixed volume reservoir where the pressure is monitored in order to allow permeability measurements. The experimental procedure involves first increasing the confining pressure and then the pore-fluid pressure in order to prevent oil penetrating the pore-fluid system, while ensuring the effective pressure never exceeded the starting conditions. Temperature was then increased up to 70 °C and when pore-fluid pressure was equilibrated, the temperature ramp and constant displacement were applied.

Table 1
List and details of the experiments conducted in this study.

Run number	*PP* (MPa)	*PC* (MPa)	Velocity ($\mu m\,s^{-1}$)	Friction (μ_s)	Max $\Delta\tau$ (MPa)	Max ΔPP measured (MPa)	Max ΔPP computed (MPa)	Author comments
DS23	2	52	0.1	0.68	3.1	0	4.5	Stable
DS19	2	52	0.4	0.67	5.9	0	8.8	Stable
DS29	2	102	0.1	0.58	10.7	3.4	18.4	Unstable >142 °C
DS22	2	102	0.4	0.59	9.0	2.0	15.2	Stable
DS21	2	152	0.1	0.54	29.4	14.6	54.4	Unstable >144 °C
DS20	2	152	0.4	0.54	20.7	15.3	38.3	Stable
Stop 1	2	152	0.4	0.54	–	–	–	Stable
Stop 2	2	152	0.4	0.53	–	–	–	Stable
Stop 3	2	152	0.4	0.53	18.9	7.6	35.6	Stable
Stop 4	2	152	0.4	0.53	18.5	7.4	34.9	Stable

2.2. Sample preparation

Volterra gypsum is used in our experiments as an analogue material for hydrous minerals that might be subducted and dehydrated in subduction zones. Volterra gypsum powder from alabaster blocks was crushed and dry sieved to obtain the target grain size range (75–125 μm). Gypsum powder was then quickly washed with distilled water to remove the finest grains below 75 μm. This grain size is in the range of intact Volterra gypsum grain size which is between 10 and 200 μm. Powder samples were prepared using a constant mass of 1.30 g ± 0.1 and 7 ml of distilled water. The wet powder was uniformly spread along the slider with a thickness of 1 mm over an area of 20 × 30 mm. The two slider blocks and the two associated silicon rubber spacers (Fig. 1) were wrapped in a 0.5 mm thick PTFE sheet to reduce friction between the jacket and the sliders. The samples were jacketed in a 3 mm thick Viton sleeve that prevents the confining medium from penetrating the sample. The strength of the rubber spacers and Viton jacket was within the measurement resolution of the internal force gauge (<0.1 kN). Two stainless steel porous disks with a diameter of 10 mm and a high permeability of 10^{-13} m^2 are fitted within the shear surfaces of the sliders and help to distribute pore-fluid pressure over the sample (Fig. 1). Machined v-grooves of 0.2 mm depth and 0.4 mm spacing on the slider surfaces, perpendicular to the transport direction, ensure mechanical coupling between the gypsum powder and the sliders.

2.3. Triaxial apparatus

The experimental work was carried out in a triaxial deformation apparatus located in the Rock Deformation Laboratory at the University of Liverpool. The apparatus uses low-viscosity silicon oil (10 cS) as the confining medium and distilled water as the pore fluid. Two external furnaces around the vessel are controlled by a thermocouple located at the top of the specimen (Fig. 1). The temperature gradient between the top and the bottom of the specimen is less than 2 °C. One end of the sample assembly is connected to a servo-controlled pore-fluid pump that acts as a high-sensitivity volumometer, capable of controlling the pore-fluid pressure with an accuracy of 0.01 MPa. The other end is connected to a fixed low-volume downstream reservoir where a pressure transducer records the evolution of the connected pore-fluid pressure in the sample during the experiments. The confining pressure is kept constant during experiments using a servo-controlled pump with a resolution of 0.01 MPa. Force is recorded with an internal force gauge corrected for temperature changes, and with a resolution of 0.1 kN.

2.4. Permeability measurements

The pore pressure oscillation technique was used to measure permeability evolution during deformation and dehydration (Fischer, 1992; Bernabé et al., 2006). The technique consists of applying a sinusoidal pore-fluid pressure oscillation in the upstream reservoir with the servo-controlled pump and recording the attenuation (A) and phase offset (θ) of the sinusoidal pressure wave in the fixed volume downstream reservoir which is isolated from the upstream reservoir by the sample. Further details of the technique and the processing of the signal can be found in Faulkner and Rutter (2000). This method has already been successfully applied to record permeability evolution during deformation tests (Fischer and Paterson, 1992; Mitchell and Faulkner, 2008; De Paola et al., 2009). Here, the peak-to-peak amplitude of the wave is 0.4 MPa in order to limit the effects of the effective pressure oscillation on sample deformation. The period of the oscillation varies between 90 s and 360 s and is also kept as short as possible in relation to any microstructural changes in the sample during deformation and dehydration. Indeed, the technique assumes steady-state behaviour that here can be assumed to determine the permeability between 2 and 3 wave oscillations for our oscillation periods.

Bernabé et al. (2006) re-analysed the pore pressure oscillation technique using two different dimensionless parameters η and ξ to those used by Fischer (1992). These authors showed that if the measurement apparatus has a large downstream storage compared to that of the sample, it is difficult to resolve the sample storage capacity because errors or noise in the recorded data may lead to small phase shift values θ, leading to large errors in the storage capacity. However, permeability can still be accurately determined since the dimensionless parameter η (function of permeability) is insensitive to θ when θ is near the line $\xi = 0$. In that case, Bernabé et al. (2006) proposed an approximate solution to compute permeability using the amplitude ratio A, the sample cross-section area S, the sample length L, the fluid viscosity μ and the downstream storage capacity β_d.

Here, the downstream reservoir volume (2.8×10^{-6} m^3) is much larger than the sample pore volume (6×10^{-8} m^3) assuming 10% porosity. For this particular case, permeability evolution is computed using the Bernabé et al. (2006) approximation. During permeability computation, changes in water viscosity and downstream storage capacity with temperature are taken into account. The calculation also requires a sample length and a cross section area. The length is defined here as the initial thickness of the layer (1 mm) and the cross section area as the sliding surface (20×30 mm^2) (Fig. 1). Actual permeability values might be regarded with caution since our samples are not strictly homogeneous and deform during experiments. Nevertheless, the relative permeability evolution within and between experiments, even in a heterogeneous sample, still provides important insights on the permeability evolution during reaction and deformation.

2.5. Microstructural and mineralogical analyses

In order to understand the coupling between dehydration reactions and deformation, mineralogical and microstructural analyses are conducted on deformed samples. After experiments, samples were prepared for SEM and XRD analyses. 5 samples from the repeated experiments at confining pressure of 152 MPa and velocity of 0.4 $\mu m\,s^{-1}$ were prepared at different key stage intervals (called hereafter Stops 1, 2, 3, 4 and 5) to observe the evolution of the microstructures during the experiment (Table 1). An extra sample from the experiment conducted at confining pressure of 152 MPa and velocity of 0.1 $\mu m\,s^{-1}$ was also prepared to observe the influence of velocity on the microstructures. Interrupted experiments were conducted at the maximum confining pressure since the most significant mechanical and hydraulic variations occurred at these conditions, leading us to expect the largest microstructural variations. Understanding of microstructure evolution at high confining pressure will also aid our understanding of deformation at lower confining pressure.

For SEM analyses, samples were impregnated in epoxy after being stored in a desiccator for 24 h after the experiment in order to remove moisture. Impregnated samples were then cut perpendicular to the shear plane and parallel to the transport direction, and polished with 0.3 micron alumina powder and iso-propanol to prevent calcium sulphate rehydration. Samples were then carbon coated for backscattered electron analysis and observed using a Philips XL30 scanning electron microscope at the University of Liverpool. XRD analyses were also conducted at the University of Liverpool on the 5 samples listed above. Approximately 250 mg of each sample was hand crushed to a fine powder (<53 μm) in an agate mortar and transferred to a side-loading aluminium cavity mount. Sample diffraction patterns were subsequently recorded from 5° to 35° 2θ using a Siemens D-500 X-ray powder diffractometer (fitted with a PIN diode X-ray detector) and Cu$K_{\alpha 1,2}$ radiation ($\lambda = 0.15418$ nm) generated at 40 kV and 30 mA. All X-ray intensity data were collected in step-scan mode with a step increment of 0.02° 2θ and a counting time of 2 seconds per step.

3. Results

Results from the combined mechanical, hydraulic and mineralogical analyses are presented in three sections. The first section presents the evolution of pore-fluid pressure and permeability before, during and after transient slip weakening. The second section presents the evolution of microstructures and mineralogy during the experiments. Finally, section 3 focuses on the transition from stable to unstable slip at the end of the dehydration reaction.

3.1. Dehydration reaction induces transient slip weakening

The general behaviour of all experiments is characterized by a transient decrease of the shear stress with stable slip behaviour during dehydration reaction (Fig. 2A). However fault strength recovery is documented following slip weakening showing that the dehydration reaction does not induce permanent weakening as also observed by Proctor and Hirth (2015). In the following, the influence of permeability, pore-fluid pressure and mechanism of deformation (*i.e.* brittle or viscous) on transient slip weakening are investigated. By brittle we mean pressure-sensitive and rate-independent deformation while for viscous we mean pressure-insensitive and rate-dependent deformation.

Fig. 2A and Table 1 also show that increasing confining pressure and/or decreasing strain rate, at effective confining pressure $PC_{\text{eff}} \geq 100$ MPa enhances the magnitude of transient slip weakening (*i.e.* shear stress drop during stable slip). Transient slip weakening is inversely related with pore-fluid pressure changes as shown in the downstream reservoir where incipient slip weakening correlates with the start of pore-fluid pressure increase (Fig. 2B). Also, the peak of pore-fluid pressure coincides with the lowest shear stress value and fault strength recovery coincides with a decrease of pore-fluid pressure. Conversely, transient slip weakening is correlated with permeability evolution where weakening is associated with permeability decrease and strengthening with permeability increase (Fig. 2C). In support of these observations, increase in permeability coincides also with the discharges of pore-fluid into the upstream reservoir during fault strength recovery as shown by pore-fluid volumometry (Fig. 2D). Pore-fluid pressure and permeability evolution are thus likely controlling transient slip weakening.

The onset of dehydration reaction is inferred to occur at the start of the downstream pore-fluid pressure increase and slip weakening for experiments conducted at $PC_{\text{eff}} \geq 100$ MPa. The measured permeability is low enough to limit percolation from the downstream reservoir to the upstream reservoir (Fig. 2A–B). The onset of the dehydration reaction is confirmed by SEM and XRD analyses showing bassanite at Stop 1 (see section 3.2). Before the onset of dehydration reaction, Fig. 2A shows that yield stress increases with confining pressure. Frictional (*i.e.* pressure sensitive) behaviour is thus inferred to occur at this stage. However, the values of the coefficient of friction μ_s before slip weakening decrease with increasing confining pressure indicating that deformation becomes less-pressure sensitive (Fig. 2A and Table 1). This behaviour can either be explained by a contribution of pressure-insensitive viscous deformation or by approaching the critical-state point as occurs at higher effective stress for the deformation of porous rocks (*i.e.* critical state soil mechanics). Both of these would reduce the slope the yield surface. However, the lower permeability values for a given displacement when the strain rate is reduced supports viscous deformation (Fig. 2C). Reducing strain rate gives more time for pores to compact leading to a reduction of permeability. Deformation in the experiments can therefore be viewed as quasi-frictional and controlled by a combination of frictional processes (*i.e.* brittle) and rate-dependent mechanisms (*i.e.* viscous) (Table 1). Viscous compaction could be due to some combination of pressure solution and intra-crystalline plasticity but further analysis is outside the scope of this contribution. There may also be a kinetic effect where reducing the displacement and temperature ramp rates gives more time for the reaction, as well as viscous compaction, to occur.

A change of the intrinsic strength of the material during the dehydration reaction may also influence the evolution of shear stress. Ko et al. (1995) showed that mineral change from gypsum to bassanite during dehydration reaction leads to strengthening due to bassanite being stronger than gypsum. Therefore, intrinsic strength change cannot explain the weakening observed during our experiments. In our study the maximum pore-fluid pressure measured in the downstream reservoir for the 5 repeated tests is variable despite their stress–strain curves being very similar (see tests at *PC*: 152 MPa and *V*: 0.4 $\mu m\,s^{-1}$ on Fig. 2A–B and Table 1). Some degree of undrained behaviour is thus inferred. Making this assumption, the undrained pore-fluid pressure inside the layer can be estimated assuming that the shear stress is governed by Amontons's law, with effective normal stress:

$$\tau = \mu_s(\sigma_n - \alpha Pf) \quad (1)$$

where τ is the shear stress measured with the internal force gauge, σ_n is the normal stress corresponding here to the confining pressure, Pf is the pore-fluid pressure, μ_s is the friction coefficient and α is the effective stress coefficient (assumed to be equal to one here). Assuming that the friction coefficient of the layer is equal to the ratio between shear stress and effective normal stress

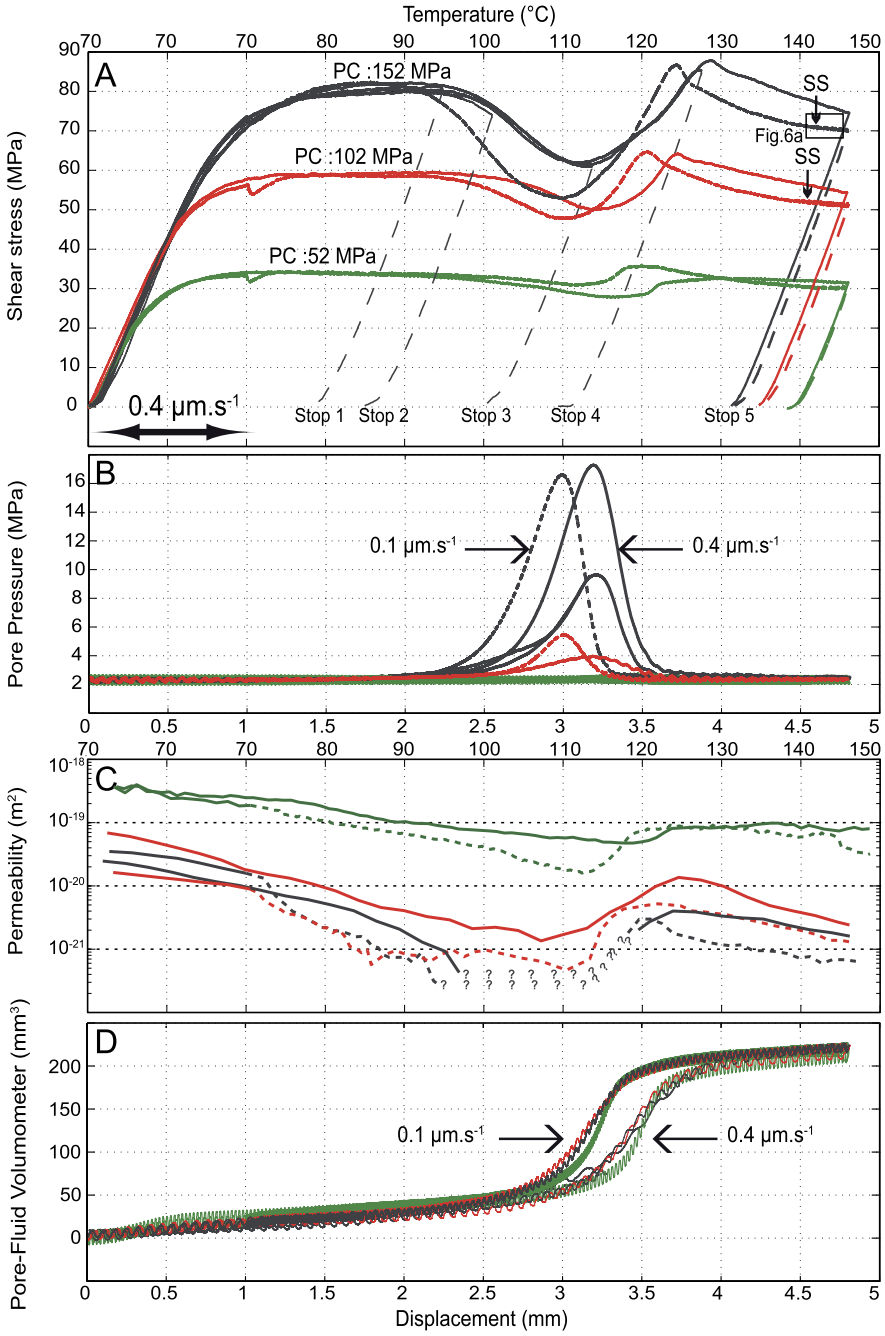

Fig. 2. Results of experiments conducted at different effective confining pressures of 50 MPa (green), 100 MPa (red) and 150 MPa (black). During the first millimetre of displacement, temperature is maintained at 70 °C and velocity at 0.4 µm s^{-1}. After 1 mm displacement, a temperature ramp is applied and axial piston velocity is either maintained at 0.4 µm s^{-1} (bold lines) or reduced to 0.1 µm s^{-1} (dashed lines). A) Evolution of shear stress during the dehydration reaction. Stops 1, 2, 3, 4 and 5 indicate experiments interrupted at different displacements which provided a set of deformed samples suitable for analysis of microstructural and mineralogy evolutions with increasing displacement and progressive dehydration of gypsum. *SS* corresponds to the inception of stick–slip events. B) Evolution of the pore-fluid pressure in the non-controlled and constant volume downstream reservoir. C) Evolution of the permeability during dehydration reaction. Question marks correspond to extrapolated permeability values due to the difficulty to compute permeability during downstream pore-fluid pressure increase. D) Evolution of the upstream reservoir volume. Oscillations correspond to the imposed pore-fluid pressure wave used for permeability measurement during the experiment. (For interpretation of the references to color in this figure legend, the reader is referred to the web version of this article.)

before dehydration, the maximum pore-fluid pressure values developed during dehydration are computed using Eq. (1) and give values higher than those measured in the downstream reservoir (Table 1). Computation of the friction coefficient can also be done assuming that the shear stress drop is only controlled by pore-fluid pressure variations measured in the downstream reservoir. Results show that the friction coefficient at the peak of pore-fluid pressure would have to drop to 0.38 which is much lower than those before the dehydration reaction. These results suggest that slip weakening is mainly controlled by unconnected overpressured fluid developed during the dehydration reaction which is greater than that measured in the downstream reservoir.

Following transient slip weakening, the shear stress exceeds that measured before dehydration starts, in agreement with bassanite being stronger than gypsum (except for experiment DS19). An overall strain weakening is recorded for these tests during this phase. For the tests at 0.1 µm s^{-1}, when the confining pressure is above 100 MPa and temperatures exceed ~140 °C, stick–slip

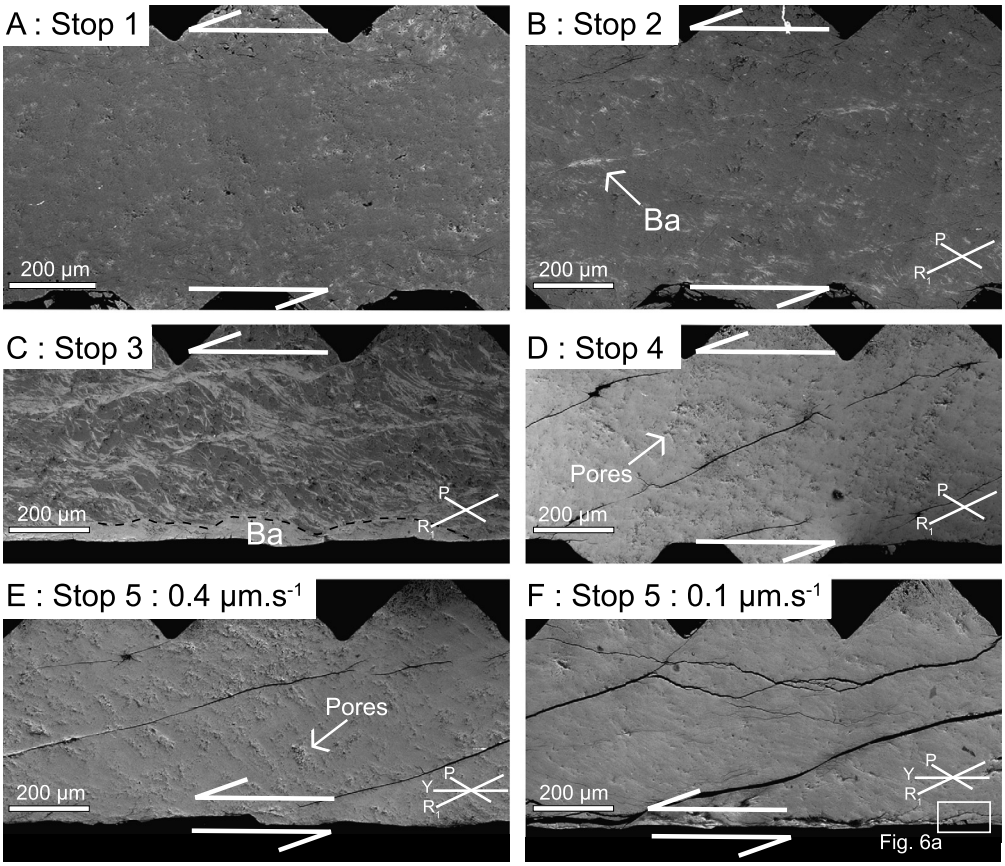

Fig. 3. Back-scattered electron SEM micrographs showing the evolution of microstructures during gypsum dehydration. Samples are oriented parallel to the transport direction and perpendicular to the layer boundaries. See Fig. 2A to locate the five stops during the experiments. Gypsum corresponds to dark grey while bassanite (*Ba*) corresponds to light grey. The general evolution of microstructures during gypsum dehydration is characterized by both bassanite and deformation located along R_1 Riedel shears and *P* foliation planes. A) Distributed deformation at the onset of gypsum dehydration (see Fig. 4A for a more detailed view). B) Preferential localization of bassanite along R_1 Riedel shears and P foliation planes during slip weakening (see Fig. 4B for a zoom). C) Bassanite is extensively localized along continuous R_1 Riedel shears and *P* foliation planes (see Fig. 4C for a zoom) and also within a thick ribbon at the drained side of the sample interpreted as a reaction front. Pore compaction associated with gypsum dehydration is shown by layer thickness decrease. D) Continuous oblique brittle R_1 shears are developed at the peak of shear stress. Pores formed during dehydration reaction are preserved within the layer (see Fig. 4D for a more detailed view). E) A narrow Y-shear is developed at the base of the layer after transient slip weakening. Pores are still preserved within the layer (see Fig. 4E for a zoom). F) Reduction of displacement rate from to 0.4 to 0.1 µm s^{-1} enhances pore compaction (see Fig. 4F for a more detailed view) and the development of Y-shears.

events are observed in the final stages of slip. Further consideration of the stable to unstable transition are presented in section 3.3 based on the mechanical and microstructural analyses.

3.2. Evolution of microstructures and mineralogy during experiments

This study includes 5 experiments which were interrupted at different and progressive values of displacement providing recovered samples suitable for microstructural and mineralogical analyses. Our set of samples allows observation of microstructural and mineralogical changes at the onset of the dehydration reaction (Stop 1), during slip weakening (Stop 2), at the onset of shear stress increase (Stop 3), at the end of transient slip weakening (Stop 4) and at completion of the dehydration reaction (Stop 5) (Figs. 3, 4 and 5). Generally, microstructural evolution is characterized by the development of R_1 Riedel shears and *P* foliation planes, and by a significant thickness decrease due to the compaction of initial pores and subsequently formed during dehydration (Fig. 3).

Stop 1 corresponds to the start of the dehydration reaction despite no discernible bassanite peak is observed in the XRD trace (Fig. 5A). It is characterized instead by the presence of needle-shaped crystals identified as bassanite (lighter mineral) in the electron backscatter image (Fig. 4A). Deformation is distributed within the simulated gypsum fault zone and preserved open pores are located between compacted gypsum aggregates (Figs. 3A and 4A).

At Stop 2, XRD analysis confirms on Fig. 5B that bassanite, despite being metastable, is the product of dehydration reaction rather than anhydrite in agreement with Hildyard et al. (2011) who also showed that bassanite forms under the experimental conditions investigated. SEM observations show that needles of bassanite are not randomly distributed in the gypsum layer but have a spatial correlation with the development of R_1 Riedel shears and *P* foliation planes (Figs. 3B and 4B). Bassanite is also preferentially located in compressional jogs with needles oriented parallel to *P* foliation planes (Fig. 4B).

At Stop 3, gypsum and bassanite co-exist within the sample in similar proportions (Fig. 5A). Bassanite is extensively developed along R_1 Riedel shears and *P* foliation planes with needles parallel to these structures (Figs. 3C and 4C). Bassanite is also located within a thick ribbon at the side of the layer near the contact with the stainless steel sliding block which is connected to the upstream reservoir (left hand side on Fig. 1, base on Fig. 3C). The development of the thick bassanite ribbon can be explained on the basis that pore-fluid pressure, not confining pressure, is the main parameter controlling reaction rate as demonstrated by Olgaard et al. (1995), Miller et al. (2003) and Llana-Fúnez et al. (2012). The upstream reservoir is maintained at constant low pore-fluid pressure, whilst elsewhere the pore-fluid pressure may build up if perme-

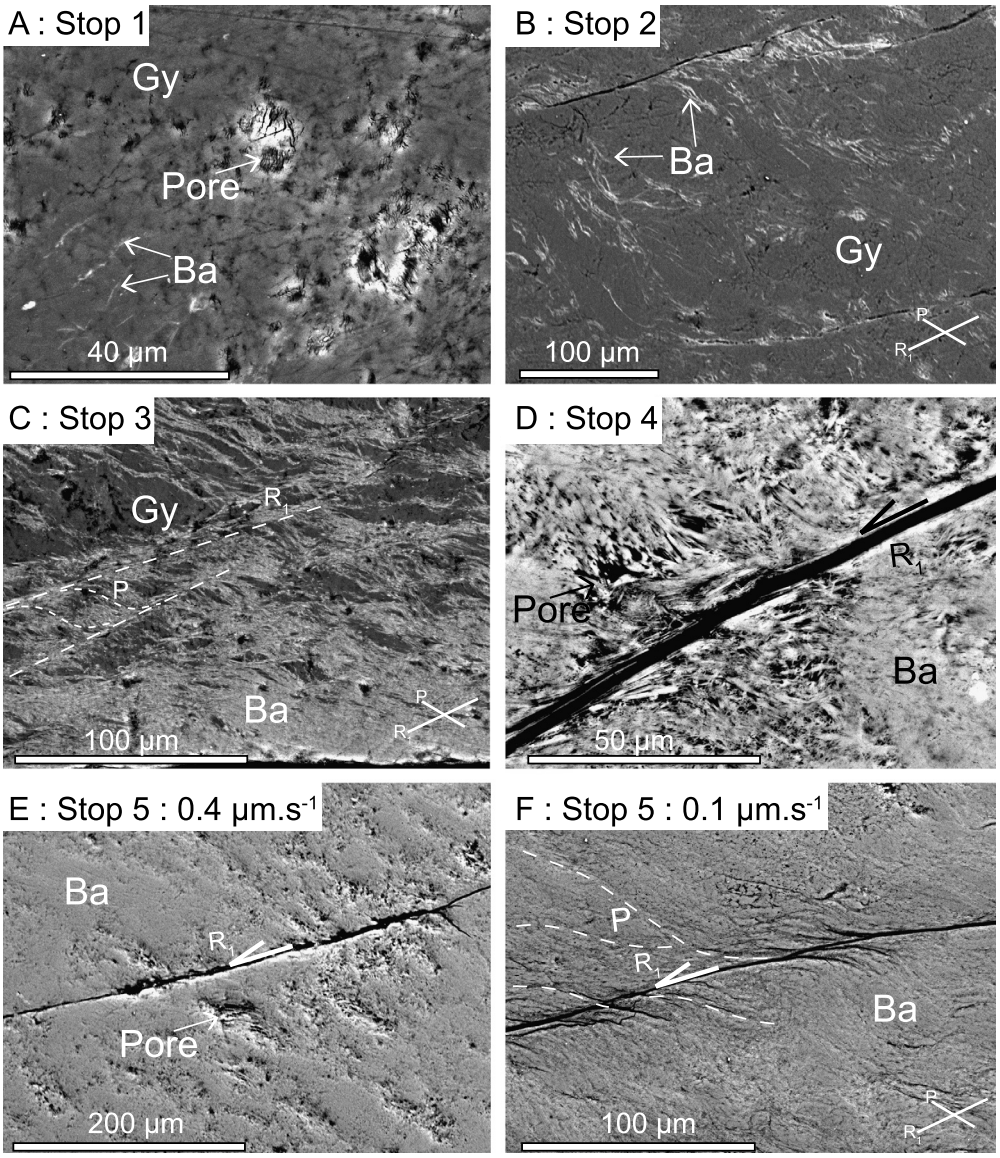

Fig. 4. Back-scattered electron SEM photo micrographs focusing on microstructures developed during gypsum dehydration and presented in Fig. 3. See Fig. 2A to locate the five stops during the experiments. *Ba*: Bassanite and *Gy*: Gypsum. A) At the onset of dehydration reaction fine bassanite needles are formed. Preserved pores are present between gypsum aggregates. B) Formation of R_1 Riedel shears and *P* foliation planes with bassanite preferentially located along these structures. Note also the preferential orientation of bassanite needles parallel to *P* foliation planes in compressional jogs. C) Intensification of bassanite localization (*i.e.* shear-related dehydration) along R_1 Riedel shears and *P* foliation planes during gypsum dehydration. D) Zoom on narrow oblique brittle R_1 Riedel shears and well-preserved pores located between bassanite needles inducing permeability increase. E–F) At the end of experiments conducted at 0.4 µm s^{-1} pores are still preserved between narrow oblique brittle R_1 Riedel shears while for experiments conducted at 0.1 µm s^{-1} pores are intensively compacted between oblique brittle R_1 Riedel shears and *P* foliation planes.

ability is low and slows down the reaction rate away from the drained boundary. The margin of this ribbon can thus be viewed as a reaction front that is moving across the sample through time towards the downstream (undrained) side.

At Stop 4, dehydration reaction is almost completed with a large proportion of bassanite replacing gypsum (Fig. 5A). The increase in bassanite content promotes the development of continuous brittle oblique R_1 Riedel shears as bassanite is mechanically stronger than gypsum (Figs. 3D and 4D). Deformation is likely accommodated by sliding along oblique R_1 shear planes controlled by the frictional properties of bassanite (Fig. 4D). Preserved pores are also observed between bassanite needles formed following the dehydration of gypsum (Fig. 4D).

At Stop 5, dehydration reaction has gone to completion as shown on XRD analysis where only bassanite peaks are present (Fig. 5A). A Y-shear plane (parallel to transport direction) is developed at the base of the layer and near the contact between steel forcing block and sample (base of Fig. 3E and Fig. 6). Oblique R_1 shear planes are still observed and do not appear deformed or to be cut by this or other Y-planes so it is difficult to establish whether or not they are still active at this stage (Fig. 4E). However, the formation of a new Y-shear plane indicates that pre-existing oblique R_1 shear planes acted as a strain hardening structure, transferring strain to a new Y-shear plane. Comparison between experiments conducted at 0.1 and 0.4 µm s^{-1} shows that the evolution of microstructures is influenced by rate-dependent deformation where a slower strain rate enhances the development of R_1 Riedel shears and *P* foliation planes, and pores compaction (Figs. 3E–F and 4E–F).

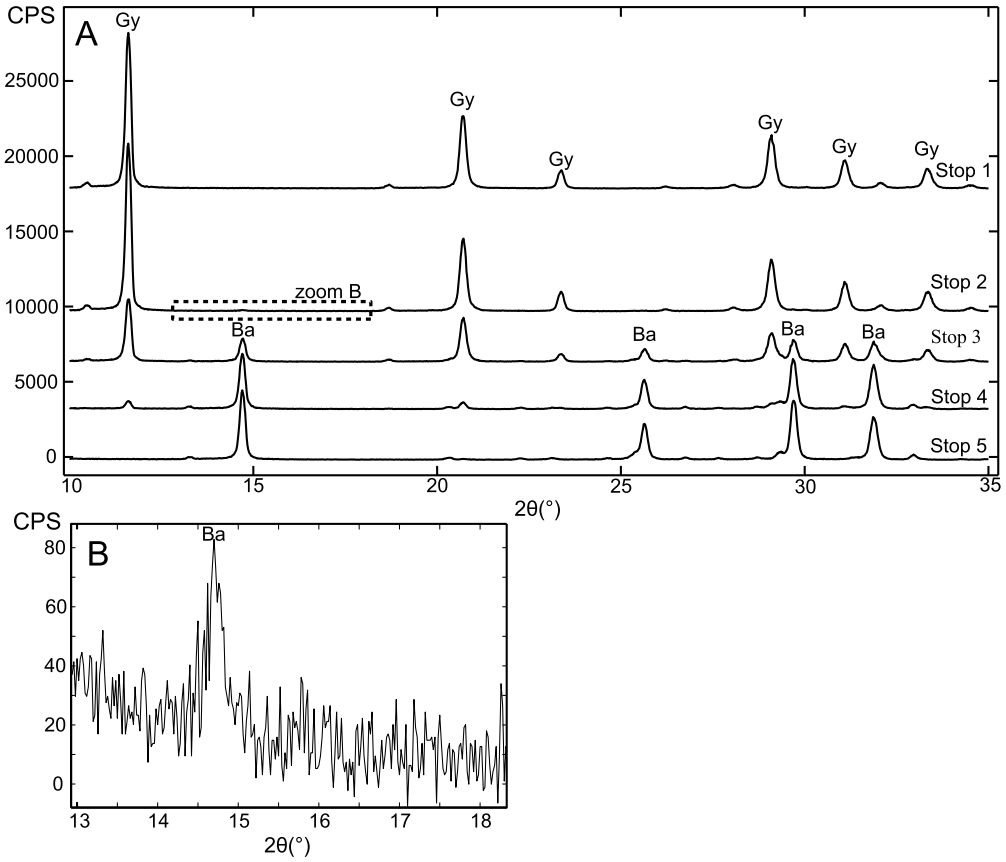

Fig. 5. XRD diffractograms for the 5 selected samples (Stops 1 to 5). A) Qualitative evolution of gypsum (*Gy*) and bassanite (*Ba*) during dehydration. B) Zoom on diffractogram at Stage 2 showing the onset of dehydration reaction by the presence of a bassanite peak.

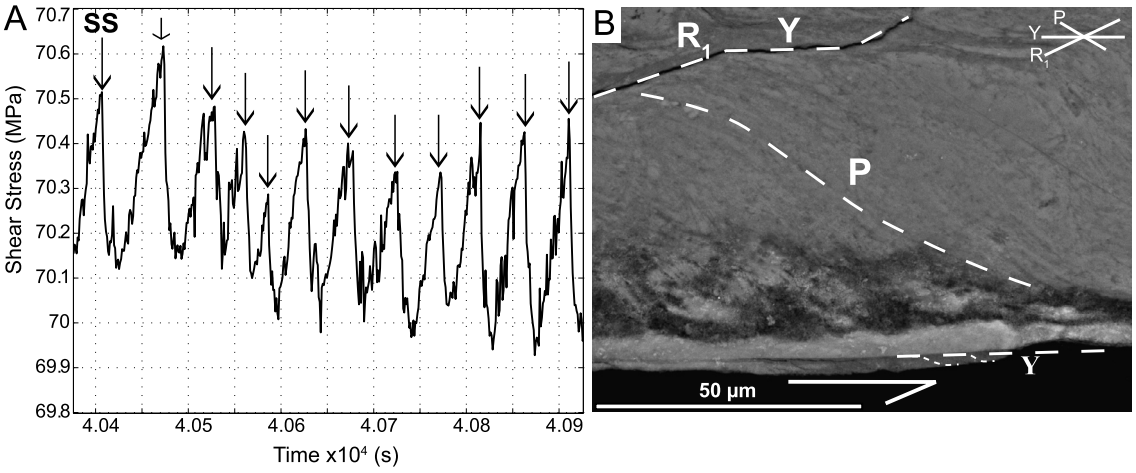

Fig. 6. Focus on the unstable slip behaviour developed at the end of gypsum dehydration characterized by stick–slip events (*SS*) localized along a basal narrow Y-shear. A) Detail on the stick–slip events developed above ~140 °C and at 0.1 µm s^{-1} during experiments DS21 (see Fig. 2 and Table 1). B) Photo micrograph of the narrow Y-shear developed at the base of the layer near the contact of the sample slider after transient slip weakening.

3.3. Transition from stable to unstable slip

Stable slip is observed all the way through transient slip weakening, including the shear-stress drop and subsequent increase. Gypsum dehydration reaction is thus accompanied by stable slip regardless of normal stress and strain rate. However, stick–slip events are observed on completion of the dehydration reaction and are promoted by higher confining pressures and lower velocities (0.1 µm s^{-1}) (Fig. 6A and Table 1). These results are different to those obtained by Takahashi et al. (2011) on antigorite gouge that showed a transition from stable sliding to unstable sliding during dehydration reaction caused by the mineralogical change from antigorite to olivine. Okazaki and Hirth (2016) also observed a transition from stable to unstable slip during lawsonite dehydration by recording acoustic emissions (*AE*). In contrast to Takahashi et al. (2011), these authors explain triggering of instabilities by the development of high pore-fluid pressure and the velocity-weakening behaviour of the reacting product. Here, the change from stable to unstable slip occurred after the dehydration reaction, at temperatures around 140 °C and is likely due

to the layer being entirely bassanite and to the increase in temperature (Fig. 2A and Table 1). Stick–slip and instability results from velocity-weakening behaviour and the stiffness of the apparatus. Hence we can infer velocity-weakening at the onset of stick–slip but the sample may have become velocity-weakening before stick–slip occurs. However, Pluymakers et al. (2014) showed that, in wet anhydrite gouge, an increase in temperature above 140–150 °C triggered a transition in frictional properties from velocity-strengthening to velocity-weakening behaviour. The transition from a stable to unstable slip can also be linked to the development of continuous Y-shear planes as shown by Scuderi et al. (2013) using a mixture of anhydrite–dolomite gouge where slip localization along continuous Y-shear plane induced an evolution from stable slip to unstable slip. In this study, no evidence for Y-planes during stable slip is observed (Stops 1–4 on Fig. 3). Conversely, a micrometre-thick Y-plane is developed during unstable slip near the contact with the steel forcing block and is consistent with the evolution from stable slip to unstable slip (Figs. 3E–F and 6B).

The stable sliding observed during transient slip weakening is thus likely controlled by the velocity-strengthening behaviour of bassanite at temperatures below ~140 °C and porosity collapse promoting distributed deformation in the regions between the R_1 Riedel shears. However, the transition from stable to unstable behaviour observed above ~140 °C and when reducing velocities from 0.4 to 0.1 $\mu m\,s^{-1}$ shows that instabilities can develop during gypsum dehydration and transient slip weakening if temperature is above around 140 °C.

4. Discussion

The discussion deals with the processes occurring during dehydration reactions and the implications of the resulting changes in the mechanical behaviour and hydraulic properties on fault mechanics. It consists of two sections. The first section proposes a conceptual model for transient slip weakening during gypsum dehydration based on the results of this study. This model includes the occurrence of shear-related dehydration and the development of a pore-fluid pressure pulse during dehydration reaction. The second section identifies and discusses the conditions required to trigger earthquakes during dehydration reaction.

4.1. Conceptual model to explain the transient slip weakening associated with dehydration

In this study, shear stress, pore-fluid pressure and permeability, in addition to microstructural and reaction progress evolution are monitored and hence the processes responsible for transient slip weakening can be more tightly constrained in comparison to the previous study of Proctor and Hirth (2015) who analysed transient slip weakening during serpentine dehydration using a Griggs apparatus without pore-fluid pressure control. The evolution of shear stress, porosity, permeability, pore-fluid pressure, reaction progress and microstructures during gypsum dehydration reaction is summarized in Fig. 7.

Below the gypsum dehydration temperature (Stage 1 on Fig. 7), samples are deformed by quasi-frictional deformation with some rate-dependent deformation, promoting overall compaction. The reduction of porosity via pore collapse results in permeability decrease. This was also seen by Wang and Wong (2003) who used a power law to model the decrease of gypsum permeability during porosity reduction.

At the onset of gypsum dehydration (Stage 2 on Fig. 7), bassanite is preferentially localized along R_1 Riedel shears and P foliation planes (*i.e.* shear-related dehydration). The preferential location of dehydrated products along Riedel shears has been previ-

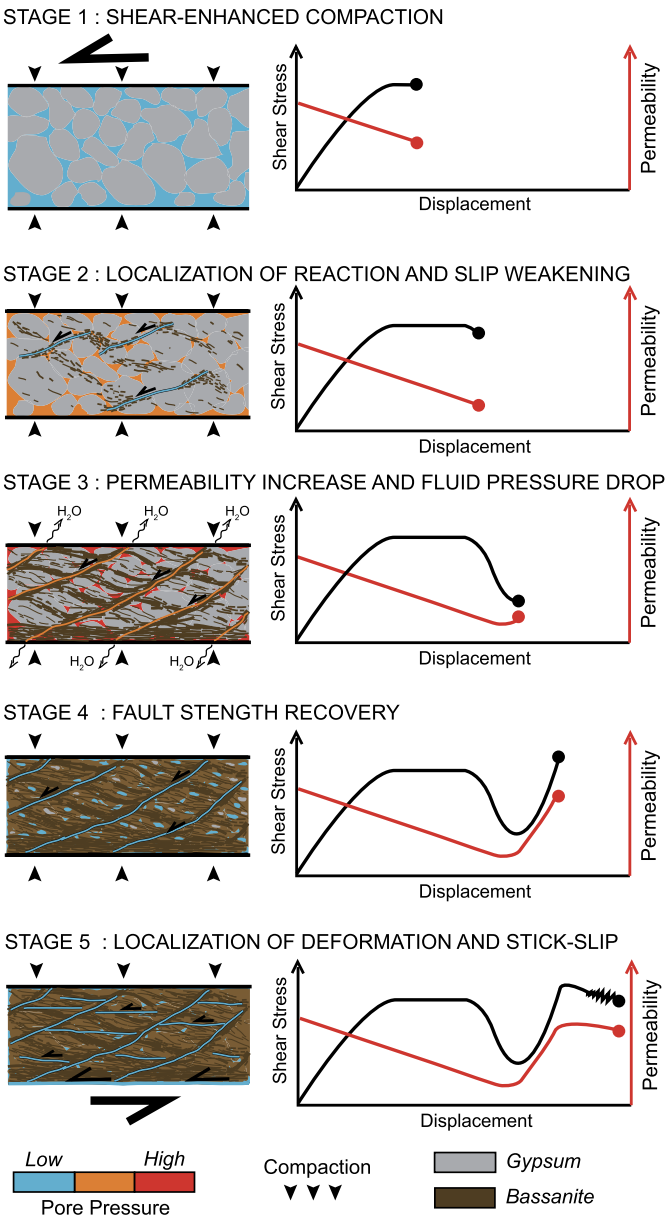

Fig. 7. Schematic conceptual model showing the evolution of microstructures, pore-fluid pressure, permeability and shear stress during gypsum dehydration. (For interpretation of the colors in this figure, the reader is referred to the web version of this article.)

ously pointed out by Takahashi et al. (2011) and Proctor and Hirth (2015) as an important parameter for understanding earthquakes linked to dehydration reactions. This preferential location may be explained by two processes. First, the reaction might be promoted by pore-fluid pressure changes where fluid-flow pathways develop preferentially at the reaction locus, locally reducing pore-fluid pressure and promoting gypsum dehydration (Olgaard et al., 1995; Llana-Fúnez et al., 2012; Brantut et al., 2012). It may also be explained by stress concentration at the locus of incipient R_1 Riedel shears and P foliation planes which locally modifies the chemical potential and triggers the reaction (*e.g.* Wheeler, 2014). Unfortunately, it is not possible to distinguish between these two mechanisms with the current dataset. At onset of gypsum dehydration, permeability is still decreasing due to the compaction of newly formed pores in relatively weak gypsum aggregates. The general permeability reduction induces then the development of pore-fluid pressure due to the combination of pore compaction

and release of free-water from gypsum dehydration. Free-water is thus accumulated, pressurized and trapped in low permeability patches. Pore-fluid pressure build-up decreases the effective normal stress and induces stable slip weakening controlled by the velocity-strengthening frictional properties of bassanite at temperature below ~140 °C.

During gypsum dehydration (Stage 3 on Fig. 7), the increase of bassanite content is still associated with the development of continuous R_1 Riedel shears and P foliation planes. The increase of bassanite content allows the progressive maintenance of newly formed pores in relatively strong bassanite aggregates inducing permeability change from decreasing to increasing. The increase of permeability above a threshold value induces then rapid fluid drainage, pore-fluid pressure drop, and promotes the onset of shear stress increase. A pulse of fluid overpressure can thus be generated in much the same way as in the fault-valve behaviour model (Sibson, 1990; Wong et al., 1997).

After the onset of fault strength recovery (Stage 4 on Fig. 7) the progressive decrease of the pore-fluid pressure enhances the reaction rate leading to an increase of bassanite content, porosity and permeability. The peak of shear stress is reached when pore-fluid overpressures are totally dissipated in the sample. The shear stress is followed by strain softening behaviour associated with the deformation being transferred and localized along newly formed Y-shear plane where the development of stick–slip events at low velocity (0.1 $\mu m\,s^{-1}$) and temperature above ~140 °C is seen (Stage 5 on Fig. 7). Unstable sliding along the Y-shear plane can be explained by the frictional properties of bassanite characterized by velocity-weakening behaviour at this stage.

4.2. What are the conditions necessary for instabilities to form in dehydrating subduction zones systems?

Dehydration reactions have been extensively analysed in the laboratory using gypsum and serpentine with high pressure (HP) (100 MPa to 8 GPa) and high temperature (HT) (105 °C to 700 °C) apparatus such as Griggs rigs, multianvil apparatus and triaxial rigs. During dehydration reactions, the development of high pore-fluid pressure has been inferred to induce embrittlement and acoustic emissions (Raleigh and Paterson, 1965; Dobson et al., 2002; Jung et al., 2004; Burlini et al., 2009; Brantut et al., 2012). Even if it is technically not possible to measure directly pore-fluid pressure inside the sample, the estimations of pore-fluid pressure from the friction data show that its evolution controls transient slip weakening in agreement with Proctor and Hirth (2015) (Table 1). Several authors proposed that fluid released by dehydration or decarbonation reactions can trigger earthquakes in the surrounding rocks during fluid drainage (Miller et al., 2004; Cappa et al., 2009; Rutter et al., 2009; Chernak and Hirth, 2011; Brantut et al., 2012). Migration of high pore-fluid pressure along subduction zones has been also suggested to be the source of creep or slow-slip events (SSE) at the plate interface due to a decrease in the locking degree by pore-fluid pressure (Moreno et al., 2014; Frank et al., 2015). Our results show that permeability increase during dehydration reaction can induce fluid migration in the form of a pulse of fluid overpressure following fault-valve type behaviour. A pressure pulse could be driven and maintained by porosity compaction following fluid drainage and reaction enhancement due to pore-fluid pressure drop as observed during our experiments and modelled by Connolly (1997).

However, the question of whether or not dehydration in subduction zones can trigger instabilities at the locus of dehydration reactions is still debated. Among the studies documenting unstable slip during dehydration reactions, the instabilities developed either in the reacting phase (*e.g.* lawsonite as shown by Okazaki and Hirth, 2016) or in the dehydrated phase (*e.g.* olivine as shown by Okazaki and Katayama, 2015 and Takahashi et al., 2011). It is thus important to understand which mineral phase (*i.e.* reacting or dehydrated) is likely to trigger an instability. If the reacting phase has a velocity-weakening behaviour, the development of high pore-fluid pressure is required to trigger an instability along localized brittle shear plane as shown by Okazaki and Hirth (2016). Similar behaviour is expected if both reacting and dehydrated phases have velocity-weakening behaviour. However, if only the dehydrating phase has a velocity-weakening behaviour, such as during antigorite dehydration, experimental studies lead to either stable or unstable slip. The key differences relate to the spatial distribution of dehydrated products and the mechanisms leading to unstable slip. At high pressure (1 GPa) and high temperature (between 400 and 700 °C), Proctor and Hirth (2015) observed a transition from localized deformation at the onset of slip weakening to distributed deformation with continued deformation at antigorite dehydration conditions. The dehydration is associated with homogeneously distributed dehydrated products in the samples that, along with distributed semibrittle deformation, are inferred to inhibit earthquake triggering. Conversely, at low effective confining pressures between 60 and 180 MPa, Takahashi et al. (2011) and Okazaki and Katayama (2015) observed a transition from stable slip to unstable slip during antigorite dehydration. These authors showed that the unstable behaviour is driven by the velocity-weakening frictional properties of olivine preferentially located along shear planes by shear-related dehydration (Boettcher et al., 2007). Another possibility is that antigorite may be velocity-weakening at these conditions, however this has not been seen during friction experiments on antigorite (Takahashi et al., 2011). While the high effective pressure conditions might be seen as more representative of those in subduction zones, the development of high pore-fluid pressures during dehydration reaction could easily lead to lower effective pressures, commensurate with those in the experiments at low effective pressure (Proctor and Hirth, 2015).

Velocity-weakening behaviour is not sufficient to guarantee instability. The stiffness of the loading system must be lower than a critical stiffness. Stiffness is defined as how rapidly the stress decreases with displacement in the surroundings of the slipping surface. In an experiment, this means the machine whereas in nature, it means the region surrounding the fault. When stiffness is lower than critical stiffness, acceleration of the system and instability result (Scholz, 2002). Proctor and Hirth (2015) report their machine stiffness as 120 kN/mm, whereas the stiffness of the apparatus used in the study of Takahashi et al. (2011) is 82 kN/mm (Okazaki and Katayama, 2015), although both these values do not account for the sample stiffness. Consequently, the stick–slip instabilities in the experiments of Takahashi et al. (2011) may be also influenced by the lower machine stiffness and care must be taken in distinguishing the intrinsic behaviour of the shearing material and the overall behaviour influenced by the loading system. In nature, the same applies. The stiffness of the subduction zone interface plays a role in the stability of slip, yet that stiffness depends on fault size and decreases as faults grow.

In order to clarify the conditions required to trigger earthquakes during dehydration, a flow diagram is proposed, based on the results presented here and previous studies described above (Fig. 8). In the flow diagram, it is assumed that velocity-strengthening material always leads to stable slip. However, numerical modelling by Brantut and Sulem (2012) has shown that velocity-strengthening material associated with reaction-weakening (*i.e.* development of pore-fluid pressure or formation of weaker dehydrated minerals) might trigger instabilities when the stiffness of loading system is below a critical value. This behaviour has not been proven yet during experiments and for simplicity is not taken into account in the flow diagram. Fig. 8 highlights the importance of (1) permeability allowing pore-fluid pressure build-up and weak-

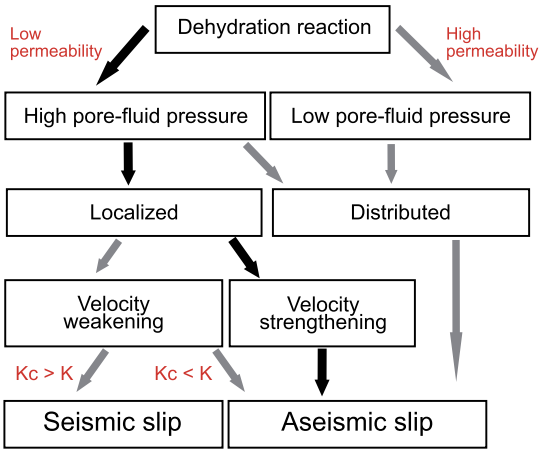

Fig. 8. Flow chart summarizing the conditions required to trigger instabilities during dehydration reactions, based on the results on this study and previous work. Localized refers to dehydrated or reacting phases located along shear planes and associated with deformation (*i.e.* shear-related dehydration) as shown by Takahashi et al. (2011), Okazaki and Katayama (2015) and Okazaki and Hirth (2016) while distributed refers to dehydrated products defining a "net structure" of interconnected reaction rims as shown by Proctor and Hirth (2015). Black arrows indicate the path followed leading to the behaviour seen in this study. K refers to the stiffness of the system loading the fault and Kc refers to the critical stiffness value.

ening, (2) the localization of deformation for instability in the reacting phase or the localization of reaction associated with deformation (*i.e.* shear-related dehydration) in the dehydrated phase and (3) the velocity-weakening behaviour of the reacting or dehydrated products leading to the nucleation of seismic events during dehydration reactions. If all these conditions are not satisfied during dehydration, stable slip will occur, as was seen in this study where bassanite was inferred to be velocity-strengthening during dehydration (black arrows on Fig. 8) or during experiments where dehydrated products and deformation were distributed during dehydration reaction, such as those of Chernak and Hirth (2010), Proctor and Hirth (2015). In the flow diagram, it is considered for simplicity that velocity-strengthening material always lead to stable slip.

5. Conclusion

In this study, evolution of pore-fluid pressure, reaction progress and permeability, in addition to the shear stress, are measured continuously during gypsum dehydration using a direct shear sample assembly. The temperature-ramp experiments conducted here show that gypsum dehydration induces transient slip weakening that is controlled by permeability and pore-fluid pressure evolution within the sample. Transient slip weakening is characterized by stable slip during gypsum dehydration followed by fault strength recovery and unstable, stick–slip behaviour on fully dehydrated material. Microstructural analyses conducted on deformed samples show clear evidence of dehydration reaction related with the development of R_1 Riedel shears and P foliation planes where bassanite is preferentially localized along these structures. The transition from stable to unstable slip is likely due to the temperature dependence of the frictional property of bassanite and the localization of deformation along Y-shear planes. Finally, this study highlights that the evolution of permeability and pore-fluid pressure during dehydration reactions associated with the localization of velocity-weakening dehydrated or reacting phases along shear planes are key parameters to trigger earthquakes during dehydration reactions.

Acknowledgements

This work is supported by Natural Environment Research Council grant NE/J008303/1. HL deeply thanks Dr S. Crowley for his assistance with XRD analyses, C. Pinnington for training in SEM techniques and assistance during microstructural analyses and G. Coughlan for maintaining and developing the experimental equipment. Review from N. Brantut and G. Hirth helped to clarify the paper.

References

Abers, G.A., Nakajima, J., van Keken, P.E., Kita, S., Hacker, B.R., 2013. Thermal–petrological controls on the location of earthquakes within subducting plates. Earth Planet. Sci. Lett. 369–370, 178–187. http://www.sciencedirect.com/science/article/pii/S0012821X1300143X.

Bernabé, Y., Mok, U., Evans, B., 2006. A note on the oscillating flow method for measuring rock permeability. Int. J. Rock Mech. Min. Sci. 43 (2), 311–316. http://www.sciencedirect.com/science/article/pii/S1365160905000663.

Boettcher, M.S., Hirth, G., Evans, B., 2007. Olivine friction at the base of oceanic seismogenic zones. J. Geophys. Res., Solid Earth 112 (B1), B01205. http://onlinelibrary.wiley.com/doi/10.1029/2006JB004301/abstract.

Brantut, N., Schubnel, A., David, E.C., Héripré, E., Guéguen, Y., Dimanov, A., 2012. Dehydration-induced damage and deformation in gypsum and implications for subduction zone processes. J. Geophys. Res., Solid Earth 117 (B3), B03205. http://onlinelibrary.wiley.com/doi/10.1029/2011JB008730/abstract.

Brantut, N., Sulem, J., 2012. Strain localization and slip instability in a strain-rate hardening, chemically weakening material. J. Appl. Mech. 79 (3), 031004. http://dx.doi.org/10.1115/1.4005880.

Burlini, L., Di Toro, G., Meredith, P., 2009. Seismic tremor in subduction zones: rock physics evidence. Geophys. Res. Lett. 36 (8), L08305. http://onlinelibrary.wiley.com/doi/10.1029/2009GL037735/abstract.

Cappa, F., Rutqvist, J., Yamamoto, K., 2009. Modeling crustal deformation and rupture processes related to upwelling of deep CO_2-rich fluids during the 1965–1967 Matsushiro earthquake swarm in Japan. J. Geophys. Res., Solid Earth 114 (B10), B10304. http://onlinelibrary.wiley.com/doi/10.1029/2009JB006398/abstract.

Chernak, L.J., Hirth, G., 2010. Deformation of antigorite serpentinite at high temperature and pressure. Earth Planet. Sci. Lett. 296 (1–2), 23–33. http://www.sciencedirect.com/science/article/pii/S0012821X10002815.

Chernak, L.J., Hirth, G., 2011. Syndeformational antigorite dehydration produces stable fault slip. Geology 39 (9), 847–850. http://geology.geoscienceworld.org/content/39/9/847.

Collettini, C., De Paola, N., Faulkner, D.R., 2009. Insights on the geometry and mechanics of the Umbria–Marche earthquakes (Central Italy) from the integration of field and laboratory data. Tectonophysics 476 (1–2), 99–109. http://www.sciencedirect.com/science/article/pii/S004019510800396X.

Connolly, J.A.D., 1997. Devolatilization-generated fluid pressure and deformation-propagated fluid flow during prograde regional metamorphism. J. Geophys. Res., Solid Earth 102 (B8), 18149–18173. http://onlinelibrary.wiley.com/doi/10.1029/97JB00731/abstract.

De Paola, N., Faulkner, D.R., Collettini, C., 2009. Brittle versus ductile deformation as the main control on the transport properties of low-porosity anhydrite rocks. J. Geophys. Res., Solid Earth 114 (B6), B06211. http://onlinelibrary.wiley.com/doi/10.1029/2008JB005967/abstract.

Dobson, D.P., Meredith, P.G., Boon, S.A., 2002. Simulation of subduction zone seismicity by dehydration of serpentine. Science 298 (5597), 1407–1410. http://www.sciencemag.org/content/298/5597/1407.

Faulkner, D.R., Rutter, E.H., 2000. Comparisons of water and argon permeability in natural clay-bearing fault gouge under high pressure at 20 °C. J. Geophys. Res., Solid Earth 105 (B7), 16415–16426. http://onlinelibrary.wiley.com/doi/10.1029/2000JB900134/abstract.

Fischer, G.J., 1992. Chapter 8 The determination of permeability and storage capacity: pore pressure oscillation method. In: Evans, B., Wong, T.-F. (Eds.), Fault Mechanics and Transport Properties of Rocks: A Festschrift in Honor of W.F. Brace. In: Int. Geophys. Ser., vol. 51. Academic Press, pp. 187–211. http://www.sciencedirect.com/science/article/pii/S0074614208628235.

Fischer, G.J., Paterson, M.S., 1992. Chapter 9 Measurement of permeability and storage capacity in rocks during deformation at high temperature and pressure. In: Evans, B., Wong, T.-F. (Eds.), Fault Mechanics and Transport Properties of Rocks: A Festschrift in Honor of W.F. Brace. In: Int. Geophys. Ser., vol. 51. Academic Press, pp. 213–252. http://www.sciencedirect.com/science/article/pii/S0074614208628247.

Frank, W.B., Shapiro, N.M., Husker, A.L., Kostoglodov, V., Bhat, H.S., Campillo, M., 2015. Along-fault pore-pressure evolution during a slow-slip event in Guerrero, Mexico. Earth Planet. Sci. Lett. 413, 135–143. http://www.sciencedirect.com/science/article/pii/S0012821X14008127.

Hacker, B.R., Peacock, S.M., Abers, G.A., Holloway, S.D., 2003. Subduction factory 2. Are intermediate-depth earthquakes in subducting slabs linked to metamorphic dehydration reactions? J. Geophys. Res., Solid Earth 108 (B1), 2030. http://onlinelibrary.wiley.com/doi/10.1029/2001JB001129/abstract.

Hilairet, N., Reynard, B., Wang, Y., Daniel, I., Merkel, S., Nishiyama, N., Petitgirard, S., 2007. High-pressure creep of serpentine, interseismic deformation, and initiation of subduction. Science 318 (5858), 1910–1913. http://www.sciencemag.org/content/318/5858/1910.

Hildyard, R.C., Llana-Fúnez, S., Wheeler, J., Faulkner, D.R., Prior, D.J., 2011. Electron backscatter diffraction (EBSD) analysis of bassanite transformation textures and crystal structure produced from experimentally deformed and dehydrated gypsum. J. Petrol. 52 (5), 839–856. http://petrology.oxfordjournals.org/content/52/5/839.

Jung, H., Green Ii, H.W., Dobrzhinetskaya, L.F., 2004. Intermediate-depth earthquake faulting by dehydration embrittlement with negative volume change. Nature 428 (6982), 545–549. http://www.nature.com/nature/journal/v428/n6982/full/nature02412.html.

Ko, S.-C., Olgaard, D.L., Briegel, U., 1995. The transition from weakening to strengthening in dehydrating gypsum: evolution of excess pore pressures. Geophys. Res. Lett. 22 (9), 1009–1012. http://onlinelibrary.wiley.com/doi/10.1029/95GL00886/abstract.

Ko, S.-C., Olgaard, D.L., Wong, T.-F., 1997. Generation and maintenance of pore pressure excess in a dehydrating system 1. Experimental and microstructural observations. J. Geophys. Res., Solid Earth 102 (B1), 825–839. http://onlinelibrary.wiley.com/doi/10.1029/96JB02485/abstract.

Leclère, H., Cappa, F., Faulkner, D., Fabbri, O., Armitage, P., Blake, O., 2015. Development and maintenance of fluid overpressures in crustal fault zones by elastic compaction and implications for earthquake swarms. J. Geophys. Res., Solid Earth 120, 4450–4473. http://onlinelibrary.wiley.com/doi/10.1002/2014JB011759/abstract.

Llana-Fúnez, S., Wheeler, J., Faulkner, D.R., 2012. Metamorphic reaction rate controlled by fluid pressure not confining pressure: implications of dehydration experiments with gypsum. Contrib. Mineral. Petrol. 164 (1), 69–79. http://link.springer.com/article/10.1007/s00410-012-0726-8.

Miller, S.A., Collettini, C., Chiaraluce, L., Cocco, M., Barchi, M., Kaus, B.J.P., 2004. Aftershocks driven by a high-pressure CO_2 source at depth. Nature 427 (6976), 724–727.

Miller, S.A., van der Zee, W., Olgaard, D.L., Connolly, J.A.D., 2003. A fluid-pressure feedback model of dehydration reactions: experiments, modelling, and application to subduction zones. Tectonophysics 370 (1–4), 241–251. http://www.sciencedirect.com/science/article/pii/S0040195103001896.

Milsch, H.H., Scholz, C.H., 2005. Dehydration-induced weakening and fault slip in gypsum: implications for the faulting process at intermediate depth in subduction zones. J. Geophys. Res., Solid Earth 110 (B4), B04202. http://onlinelibrary.wiley.com/doi/10.1029/2004JB003324/abstract.

Mitchell, T.M., Faulkner, D.R., 2008. Experimental measurements of permeability evolution during triaxial compression of initially intact crystalline rocks and implications for fluid flow in fault zones. J. Geophys. Res., Solid Earth 113 (B11), B11412. http://onlinelibrary.wiley.com/doi/10.1029/2008JB005588/abstract.

Moreno, M., Haberland, C., Oncken, O., Rietbrock, A., Angiboust, S., Heidbach, O., 2014. Locking of the Chile subduction zone controlled by fluid pressure before the 2010 earthquake. Nat. Geosci. 7 (4), 292–296. http://www.nature.com/ngeo/journal/v7/n4/abs/ngeo2102.html.

Nakajima, J., Tsuji, Y., Hasegawa, A., Kita, S., Okada, T., Matsuzawa, T., 2009. Tomographic imaging of hydrated crust and mantle in the subducting Pacific slab beneath Hokkaido, Japan: evidence for dehydration embrittlement as a cause of intraslab earthquakes. Gondwana Res. 16 (3–4), 470–481. http://www.sciencedirect.com/science/article/pii/S1342937X0800186X.

Okazaki, K., Hirth, G., 2016. Dehydration of lawsonite can directly trigger earthquakes in subducting oceanic crust. Nature 530, 81–84. http://dx.doi.org/10.1038/nature16501.

Okazaki, K., Katayama, I., 2015. Slow stick–slip of antigorite serpentinite under hydrothermal conditions as a possible mechanism for slow earthquakes. Geophys. Res. Lett. 42, 1099–1104. http://onlinelibrary.wiley.com/doi/10.1002/2014GL062735/abstract.

Olgaard, D.L., Ko, S.-C., Wong, T.-f., 1995. Deformation and pore pressure in dehydrating gypsum under transiently drained conditions. Tectonophysics 245 (3–4), 237–248. http://www.sciencedirect.com/science/article/pii/0040195194002374.

Peacock, S.M., 2001. Are the lower planes of double seismic zones caused by serpentine dehydration in subducting oceanic mantle? Geology 29 (4), 299–302. http://geology.geoscienceworld.org/content/29/4/299.

Pluymakers, A.M., Samuelson, J.E., Niemeijer, A.R., Spiers, C.J., 2014. Effects of temperature and CO_2 on the frictional behavior of simulated anhydrite fault rock. J. Geophys. Res., Solid Earth 119, 8728–8747. http://onlinelibrary.wiley.com/doi/10.1002/2014JB011575/abstract.

Proctor, B., Hirth, G., 2015. Role of pore fluid pressure on transient strength changes and fabric development during serpentine dehydration at mantle conditions: implications for subduction-zone seismicity. Earth Planet. Sci. Lett. 421, 1–12. http://www.sciencedirect.com/science/article/pii/S0012821X15001892.

Raleigh, C.B., Paterson, M.S., 1965. Experimental deformation of serpentinite and its tectonic implications. J. Geophys. Res. 70 (16), 3965–3985. http://onlinelibrary.wiley.com/doi/10.1029/JZ070i016p03965/abstract.

Rutter, E., Llana-Fúnez, S., Brodie, K., 2009. Dehydration and deformation of intact cylinders of serpentinite. J. Struct. Geol. 31 (1), 29–43. http://www.sciencedirect.com/science/article/pii/S0191814108001624.

Scholz, C.H., 2002. The Mechanics of Earthquakes and Faulting, 2nd edition. Cambridge University Press, Cambridge Books Online.

Scuderi, M.M., Niemeijer, A.R., Collettini, C., Marone, C., 2013. Frictional properties and slip stability of active faults within carbonate–evaporite sequences: the role of dolomite and anhydrite. Earth Planet. Sci. Lett. 369–370, 220–232. http://www.sciencedirect.com/science/article/pii/S0012821X13001453.

Shimamoto, T., 1986. Strengthening of phyllosilicate and gypsum gouges with increasing temperature: effect of temperature or moisture elimination? Int. J. Rock Mech. Min. Sci. Geomech. Abstr. 23 (6), 439–443. http://www.sciencedirect.com/science/article/pii/0148906286923090.

Sibson, R.H., 1990. Conditions for fault-valve behaviour. Geol. Soc. (Lond.) Spec. Publ. 54 (1), 15–28. http://sp.lyellcollection.org/content/54/1/15.

Sleep, N.H., Blanpied, M.L., 1992. Creep, compaction and the weak rheology of major faults. Nature 359 (6397), 687–692. http://www.nature.com/nature/journal/v359/n6397/abs/359687a0.html.

Takahashi, M., Uehara, S.-I., Mizoguchi, K., Shimizu, I., Okazaki, K., Masuda, K., 2011. On the transient response of serpentine (antigorite) gouge to stepwise changes in slip velocity under high-temperature conditions. J. Geophys. Res., Solid Earth 116 (B10), B10405. http://onlinelibrary.wiley.com/doi/10.1029/2010JB008062/abstract.

Verberne, B.A., Bresser, J.H.P.D., Niemeijer, A.R, Spiers, C.J., de Winter, D.A.M., Plümper, O., 2013. Nanocrystalline slip zones in calcite fault gouge show intense crystallographic preferred orientation: crystal plasticity at sub-seismic slip rates at 18–150 °C. Geology 41 (8), 863–866. http://geology.geoscienceworld.org/content/41/8/863.

Wang, W.-H., Wong, T.-f., 2003. Effects of reaction kinetics and fluid drainage on the development of pore pressure excess in a dehydrating system. Tectonophysics 370 (1–4), 227–239. http://www.sciencedirect.com/science/article/pii/S0040195103001884.

Wheeler, J., 2014. Dramatic effects of stress on metamorphic reactions. Geology 42 (1), 647–650. http://geology.gsapubs.org/content/early/2014/06/09/G35718.1.

Wong, T.-F., Ko, S.-C., Olgaard, D.L., 1997. Generation and maintenance of pore pressure excess in a dehydrating system 2. Theoretical analysis. J. Geophys. Res., Solid Earth 102 (B1), 841–852. http://onlinelibrary.wiley.com/doi/10.1029/96JB02484/abstract.